

Supplemental Material

Ferric iron triggers greenalite formation in simulated Archean seawater

Isaac L. Hinz, Christine Nims, Samantha Theuer, Alexis S. Templeton, Jena E. Johnson

EXPERIMENTAL METHODS

Solution Preparation:

Experiments were performed in 500 mL borosilicate glass bottles at room temperature (25 °C) using 18.2 MΩ-cm ultrapure water. Ultrapure water was first boiled and purged with pure N₂ gas for initial deoxygenation and was then stirred uncapped for 48 hours in an MBraun glovebox (N₂ atmosphere with < 0.1 ppm O₂) to eliminate any residual oxygen. All chemical reagents, including the ferrous and ferric chloride, bicarbonate, seawater salts, silica, hydrochloric acid (HCl), and sodium hydroxide (NaOH) stock solutions, were weighed outside of the glovebox and then transferred to the glovebox for dissolution in the de-oxygenated water.

The artificial seawater (Table S1) solution chemistry was determined by previous estimates of salt concentrations for Archean seawater and adapted with modern seawater chemistry to target the remaining constituents. We assume relatively constant salinity over time, so sodium chloride and potassium chloride were added at approximate modern ocean concentrations of 400 mM and 7 mM respectively (Riley and Chester, 1971). We used 22 mM sodium bicarbonate as an inorganic buffer based on the estimated range of inorganic carbon (5 to 30 mM) for the Archean ocean constrained by calcium isotopic data (Blättler et al., 2017). Our seawater solution contained 10 mM ammonium chloride based on Archean seawater estimates (0.03 - 10 mM, Stüeken, 2016). Aqueous magnesium concentration in the Archean ocean is poorly constrained. Higher seawater-crust hydrothermal interactions (Spencer and Hardie, 1990; Halevy and Bachan, 2017) likely diminished the magnesium concentration in the early ocean, so we supplemented experiments with 20 mM Mg given the predicted range of 10-30 mM in Jones et al. (Jones et al., 2015). As detailed in the main text, dissolved silica in the Archean ocean has been estimated from ~0.67 mM to 1.9 mM (Siever, 1992; Maliva et al., 2005; Stefurak et al., 2015); we therefore supplied the artificial Archean seawater solution with 1 mM silica to keep solutions within the estimated range but below amorphous silica saturation (~1.9 mM; Gunnarsson and Arnórsson, 2000). Iron (100% ferrous chloride or 95% ferrous chloride and 5% ferric chloride) was added at 1 mM, both within the range of iron predicted in the Archean ocean by Jiang and Tosca (2019) and at a sufficient concentration to produce harvestable quantities of iron precipitates for our analyses.

All experiments were performed as concurrent duplicates within the glovebox (a third replicate was also performed at pH 7 with 5% Fe[III]/FeTotal). An initial 1 mM sodium orthosilicate (Na₄SiO₄, Alfa Aesar CAS: 13172-30-5) was added to 480 mL of ultrapure water, which was subsequently adjusted to the final experimental pH of 6.5-7.5 (ThermoFisher Orion Star A221 pH meter) by the dropwise addition of sodium hydroxide and/or hydrochloric acid. Next, we stirred the solution for 24 hours to ensure the depolymerization of the dissolved silica (Dietzel, 2000). Seawater salts (Table S1) were added post-silica depolymerization step, and the pH was temporarily adjusted to pH 2 to prevent any pH-driven precipitation of iron (1 mM Fe[II] or 0.95 mM Fe[II] and 0.05 mM Fe[III]). In addition to lowering solution pH during iron addition, ferric chloride was added from a highly acidic (pH ~0) stock solution to introduce Fe[III] as Fe³⁺_(aq). The solution was then brought to pH 5 by NaOH, and sodium bicarbonate (22 mM) was added slowly while maintaining pH 5 by HCl additions to both limit CO₂ outgassing and avoid exceeding the final experimental pH. Finally, we set the 500 mL experimental solutions to final pH [6.5-7.5] values, removed stir bars, and sealed bottles with rubber stoppers. All experimental bottles were wrapped in aluminum foil to eliminate potential photooxidation of ferrous iron and were allowed to

precipitate and equilibrate undisturbed for 5 days at 25 °C in the glovebox. The pH of each experiment was not measured after 5 days at 25 °C or after high-temperature aging.

Subsampling and High-temperature Aging:

After 5 days of low-temperature reaction (25 °C) and equilibration, the experiments were subsampled for subsequent analyses (liquid and solid) or for secondary hydrothermal aging. In preparation for various chemical assays, we filtered approximately 10 mL of solution from each experimental condition through cellulose acetate filters (ThermoFisher Titan 3, 0.20 µm) in the glovebox. We subsampled 25 °C precipitates by harvesting a portion of the total experimental solid in epitubes. Each harvested solid was rinsed three times in circumneutral anoxic water via centrifugation and resuspension to thoroughly remove adsorbed or extraneous salts. Following removal of the supernatant, we anoxically sealed the epitubes containing concentrated pelleted precipitates in mylar bags from each 25 °C experimental condition with sufficient material and transferred them to the -80 °C freezer to limit any further reaction prior to analysis. The presence of high silica in solution should limit the autooxidation of Fe(II)-bearing phases (Kinsela et al., 2016). Replicate experiments of each condition were performed in order to measure the total solid mass of precipitates produced at 25 °C.

The majority of the total experimental precipitate, however, was aged at 150 °C. We deposited 12 mL of the original experimental solution precipitates into anoxically sealed 22 mL gas-tight Parr vessels. In a procedure modified after (Mizutani et al., 1991) and simulating ~100 Ma of burial diagenesis (Siever, 1983) with the aim of increasing crystallinity of the solid phase(s), the vessels were placed in an oven to be aged undisturbed (not shaking) at 150 °C. After 5 days, the Parr vessels were removed from the oven and returned to the glovebox to cool. Aged precipitates were similarly rinsed three times by centrifugation to remove dissolved salts. After decanting the supernatant, we stored epitubes of hydrothermally-aged precipitates in sealed, airtight mylar bags at -80 °C pending characterization.

ANALYTICAL METHODS

Mass Measurements:

An identical set of experiments at each pH and controls (i.e. experiments supplemented with seawater salts but without iron or silica) were aged for 5 days at 25 °C. Precipitates were extracted using a vacuum filtration system with a Millipore 0.2 µm polycarbonate filter in the glovebox. Filters with captured precipitates were first dried under vacuum for 1 minute to remove excess water and were subsequently air dried for 12 hours in the glovebox (< 0.1 ppm O₂). Finally, individual dried filters were sealed in Ball glass jars and transported out of the glovebox for mass measurements using a benchtop Mettler Toledo XS105 Dual-Range balance (± 0.01 mg). The average mass of the filter paper was calculated from the control filters and subtracted from the experimental measurements presented in Table 1. The low masses in ferrous experiments (Table 1) were likely due to adsorbed water that had not yet dried or adsorbed Fe[II] that reacted to form iron oxides upon weighing in air.

Colorimetric Assays for Fe[II,III] and [Si]:

We performed the ferrozine assay (Stookey, 1970; Viollier et al., 2000) to determine Fe[III]/FeT in the precipitates [at 25 °C and after 150 °C aging] and the remaining Fe[II] in solution after 5 days at 25 °C. Ferrozine results are reported in Table 1. The assay was first conducted with ferrous chloride and ferric chloride standards [2.5-100 µM] in 0.4 M HCl to produce a standard absorbance curve using a ThermoScientific Genesys 50 UV-Visible Spectrophotometer set at 562 nm. Each experimental solution was subsampled after 5 days and acidified with 0.4 M HCl and then diluted by a factor of 10. Experimental precipitates from Fe[III]-bearing experiments were subsampled as a 2 µL slurry and then fully dissolved by

0.4 M HCl acid prior to Fe[III]/FeT determination by the Ferrozine assay. All subsamples were diluted to ensure absorbance measurements would plot within the range of the standard curves. The calculated concentrations along with their corresponding standard deviations of dissolved Fe[II] and Fe[III]/FeT for each condition are presented in Table 1.

We determined the remnant dissolved silica after 5 days at 25 °C using the silicomolybdate assay (ASTM D859-16, 2000). This assay was performed with sodium orthosilicate standards [5-100 µM] to create a standard curve from the absorbances collected on a ThermoScientific Genesys 50 UV-Visible Spectrophotometer (640 nm). Subsamples were diluted 10x in ultrapure water so the measured absorbances fit within the standard curve range. The concentration of silica was calculated from each experimental condition and presented in Table 1.

Bulk Mineralogy: Co-XRD

Approximately 1 cm of concentrated precipitate gel from each experiment containing 5% Fe[III]/FeT at 25°C and aged at 150°C for 5 days was pipetted into a Cole-Parmer Kapton tube (inner diameter, 1.46 mm with a 0.05 mm wall thickness). Kapton tubes were heat sealed in the glovebox, and were then stored in anoxic mylar bags housed in the glovebox prior to shipment to the McMaster Analytical X-Ray Diffraction Facility (MAX) for X-ray diffraction (XRD). Samples were analyzed on a Bruker D8 DISCOVER cobalt source tube XRD with a DAVINCI.DESIGN diffractometer using: 35 kV, 45 mA, 1mm slit, 1 mm collimator, and a VÅNTEC-500 area detector with a 20 cm working distance. Each sample scan included 4 frames (900 seconds per frame) at 3 separate sample areas over a 2θ range of 10-88°. The 2D frames were collected with DIFFRAC.MEASUREMENT Centre Version 6.5 software, and patterns were integrated to 1D using DIFFRAC.EVA Version 4.2. Each experiment containing 5% Fe[III]/FeT at 25°C and aged at 150°C for 5 days was analyzed once for bulk mineralogy by XRD. The experimental condition with ferrous iron at 150°C for 5 days did not produce enough material for analysis by XRD. Figure S4 compares the experimental diffraction patterns with relevant mineral standards obtained from the RRUFF database, the ICDD database, an internal lab standard verified by XRD, and patterns reported in previous publications (Figure S4 caption for source reference).

Scanning Electron Microscopy (SEM):

To analyze our experimental products at a micron-scale, we thawed and resuspended precipitates in ultrapure water. We pipetted 15 µL of precipitate slurry onto double-sided carbon tape mounted on aluminum stubs. Precipitates air dried for several hours in a stub holder in the glovebox. Dried stubs were removed from the glovebox, and were quickly transported to the Denton Desk II Au/gold sputter coater (30 seconds or ~100 Å coating on 150 °C samples; and 60 seconds for 25 °C samples). Samples were immediately analyzed to minimize oxidation. We collected secondary electron images using a JEOL JSM-7800F scanning electron microscope (SEM) with an accelerating voltage of 5 or 10 kV based on fragility and charging of the sample under the beam. Elemental data (point and map data acquisitions) were captured with an Oxford XMaxN 80mm² silicon-drift energy-dispersive X-ray spectrometer (EDS) detector and processed with Oxford Aztec v3.3 software. Precipitates at each experimental condition (5% Fe[III]/FeT at 25°C and aged at 150°C for 5 days and Fe[II] aged at 150°C) were analyzed once by SEM. Multiple regions within each sample were imaged to document reoccurring morphological features and record the chemical composition by EDS.

Transmission Electron Microscopy (TEM)-Based Analyses:

For TEM analyses, a 12 µL droplet of thawed 25 °C or 150 °C precipitate slurry, resuspended in ultrapure anoxic water, was deposited onto a carbon-coated 300 mesh copper grid (Electron Microscopy

Sciences) in the glovebox. We allowed precipitates to dry on the grids under anoxic conditions for 45 minutes, and then stored the grids in holders sealed in mylar bags before transport to analytical facilities.

We characterized the precipitates at three separate electron microscopy facilities. We used a Talos F200X G2 S/TEM (point resolution 0.25 nm, line resolution 0.12 nm, STEM < 0.16 nm, Super-X window-less EDS detector, 200keV, and Gatan OneView 4K camera) and a JEOL 2010F (0.25 nm point resolution, 0.10 nm lattice resolution, EDAX detector, 200keV, and Gatan OneView 4K camera) at the Michigan Center for Materials Characterization at the University of Michigan. Samples were also analyzed at the Center for Advanced Microscopy at Michigan State University with a JEOL 2200 FS (high-resolution imaging up to 0.19 nm, STEM 0.136 nm resolution, 200 keV). The majority of the samples, however, were analyzed at the Electron Microscopy Laboratory at Colorado School of Mines on a Talos F200X (high-resolution imaging up to 0.12 nm, STEM imaging up to 0.16 nm, 200 keV, and Super-X window-less EDS detector).

We performed FFT and IFFT using Gatan DigitalMicrograph software to measure the crystal lattice d-spacing of minerals in HR-TEM images. Elemental data [Fe, Mg, Si, O, C] was captured on a Talos F200X with a Super-X EDS detector for quantitative analysis and elemental mapping. EDS maps were collected on X-ray emission lines for iron (K- α), magnesium (K), silica (K), oxygen (K), and carbon (K) for 15 minutes with 4x4 binning. EDS data was analyzed by the Cliff-Lorimer ratio method using Bruker ESPRIT software Version 1.9. Elemental quantification was ± 1 -10% of the presented values. Selected area electron diffraction (SAED) patterns were analyzed with ImageJ Version 1.52 and Adobe Illustrator 2020 Version 24.2. Samples at each experimental condition were imaged to capture distinct morphological features, measure the elemental data of these features by EDS, and provide structural characterization by SAED (Figure S3). Subsamples of each experimental condition (at least 2 separate subsamples from the duplicate experimental bottles) were analyzed by TEM. The distinct phases and elemental chemistry in each experiment were consistent at each experimental condition. A replicate experiment at pH 7 with 5% Fe[III]/FeT aged at 150 °C for 5 days was performed at a different time, and here the observed morphologies were consistent with the first round of analysis. Due to a lack of material, the experiment with ferrous iron at 150°C for 5 days was only analyzed by TEM once.

Raman Spectroscopy:

We first pipetted ~20 μ L of thawed and resuspended precipitate slurry onto glass microscope slides in the glovebox. Coverslips were placed on wet slurry samples, which were then sealed with the application of clear acrylic on all edges of the coverslip-slide boundary. We dried the sample and acrylic seal in the glovebox under anoxic conditions for 30 minutes before analysis to avoid any mineralogical alteration from oxidation. Samples were analyzed anoxically on an XploRA PLUS Raman spectrometer mounted on an Olympus BX41 microscope. We collected spectra using a 532 nm laser with 25 mW output between 60 - 1600 cm^{-1} , at 1-10% laser intensity on a 50x long working distance objective with 20 second exposures and 15 accumulations to obtain a spectral fingerprint of the precipitate structure(s). Standards of various iron-silicates, iron-bearing minerals, and carbonates assembled from the RRUFF database and internal lab mineral collections were compared to our experimental results to evaluate spectral matches.

ANALYTICAL RESULTS

Bulk Elemental Chemistry:

Strictly ferrous experiments aged for 5 days at 25 °C produced no measurable (by bulk mass, Table 1) or visible precipitate at pH 6.5 and 7 (Figure S1). Chemical assays of the experimental solutions after 5 days of precipitation and equilibration indicated that ~100% and ~85% of Fe[II] remained in solution at pH 6.5 and pH 7, respectively. Silica concentrations in the 5-day experimental solutions appeared to decrease from the initial 1 mM Si, with colorimetric assays showing Si at approximately 0.8 mM at pH 7 and 0.6 mM at pH 6.5 (Table 1). In combination with the iron concentrations, the pH 7 solution may have formed Fe-Si dissolved complexes or colloids. We attribute the more substantial decrease of Si (~43%) at pH 6.5 without any decrease in Fe[II] concentrations or visible precipitate (Figures S1, Table 1) to possible silica polymerization or the precipitation of colloidal forms, undetectable with the silicomolybdate assay (Coradin et al., 2004). Ferrous experiments at 25 °C yielded minor visible precipitation after 5 days at pH 7.5 (Figure S1). Although this precipitate was not measurable by bulk mass (Table 1), solution measurements revealed that ~30% of the initial silica and ~22% of the initial Fe[II] was incorporated into the precipitate (Table 1).

In ferric-ferrous experiments, adding 5% Fe[III]/FeT produced considerably more precipitate mass at all tested pHs than in ferrous experiments (Table 1). Additionally, we observed more visible precipitate with increasing pH at 25 °C (Figure S1), and this trend was supported by 5-day Fe[II] solution measurements of ~42% Fe depletion at pH 6.5, ~60% Fe depletion at pH 7, and ~69% Fe depletion at pH 7.5 (Table 1). Ferric experiments also had notable changes in the Fe[III]/FeT content of the bulk precipitate over the range of experimental pHs. After 5 days at 25 °C, precipitates contained ~96% Fe[III] at pH 6.5, ~89% Fe[III] at pH 7, and ~18% Fe[III] at pH 7.5 (Table 1), revealing a substantial reduction in bulk Fe[III] content as a function of pH. Upon further aging the precipitates at 150 °C for 5 days, the Fe[III]/FeT content of the bulk precipitates decreased to 60% Fe[III] at pH 6.5, 54% Fe[III] at pH 7, but increased to 30% Fe[III] at pH 7.5 (Table 1). These measurements demonstrate that ferric iron preferentially partitions into the precipitate phase, as low total ferric iron (5% Fe[III]/FeT) is concentrated into precipitates at higher proportions of 18-96% Fe[III]/FeT.

Elemental chemistry of the precipitates as measured through SEM-EDS map sum spectra suggested that magnesium content increased considerably on the bulk scale during 150 °C aging. While 25 °C precipitates contained ~0.6-0.8 atomic % Mg in ferric-ferrous experiments at all tested pHs (Figure S5A, Figure S8A, Figure S9A), subsamples of the same experimental conditions showed large increases in Mg measured by SEM-EDS after 150 °C. At pH 6.5, Mg content of bulk precipitates was 10.1 atomic % (Figure S10A), while at pH 7, Mg content had increased to 8.5% (Figure S11A). Mg in pH 7.5 samples after high-temperature aging was measured by SEM-EDS at 7.7% (Figure S6A). This high-temperature addition of Mg could be attributed to magnesite precipitation, which was observed in all high-temperature ferrous-ferric experiments (Figure S7), or could signal a greater Mg incorporation into other solid phases like silicates upon recrystallization during 150 °C aging.

Raman Spectra:

Regardless of experimental condition, Raman spectroscopy measurements of our precipitates overwhelmingly generated spectra indicative of amorphous material. The dominant broad spectral peaks resemble a lab-synthesized standard of amorphous silica (Figure S7D), suggesting our samples contain amorphous silicate bonds. However, point spectra collected on the 150 °C-aged experiments (see Figure S7D from a 5% Fe[III]/FeT experiment at pH 7.5) did present peaks diagnostic of carbonate mineral precipitates. These measurements produced a close spectral match to a magnesite standard from the RRUFF database—indicating the local high-temperature formation of magnesite.

Identification of Magnesium-rich Greenalite-like Silicate:

Under ferrous experimental conditions at pH 7.5, aged at 150 °C precipitates imaged by SEM contained abundant <100 nm rods (Figure S2A-B). HR-TEM imaging captured clusters of poorly layered curling structures <10 nm thick with common edge dislocations (Figure 1B; 1D; S2E). We recorded one instance of a crystalline structure with 7.3 Å basal spacing (Figure 1F) but no definitive silicate-like XRD pattern (Figure S4). The elemental chemistry (Figure S3) of this phase was similar to a serpentine-group clay, suggesting the formation of a proto-1:1/(Fe-Mg) silicate.

Experiments with the addition of 5% Fe[III]/FeT at pH 6.5-7.0 produced diffraction peaks after aging at 150 °C that were consistent with 7 Å silicates (Figure S4). HR-TEM confirmed the presence of well-ordered layered structures with a basal spacing of 7.3-7.4 Å (Figure 3K&Q; S10C; S11F) in multiple sample images and across 2-3 sample replicates. Areas containing many well-ordered structures produced a polynanocrystalline diffraction pattern by SAED (Figure 3J) that matched serpentine group minerals, particularly cronstedtite [2-layer iron silicate, $\text{Fe}[\text{II}]\text{Fe}[\text{III}]_3(\text{Si},\text{Fe}[\text{III}])_2\text{O}_5(\text{OH})_4$]. The structural characterization combined with the elemental chemistry of the well-ordered phase with a typical (Fe+Mg)/Si ratio of 1.6-1.8 and Fe/Mg ratio of ~1.4 at 25 °C and 0.9 at 150 °C (Figure S3) all strongly support the identification of this phase as a 2-layer high-Mg iron silicate like greenalite.

Identification of Carbonate Green Rust:

The bulk mineralogy measured by Co-XRD revealed that pH 6.5-7.0 experiments with 5% Fe[III]/FeT aged at 150 °C had a diffraction peak at ~12° and ~23° Cu 2 θ ; these lines are consistent with fougurite, a naturally occurring carbonate green rust (Figure S4). Further characterization of these experimental precipitates by SEM imaging showed ~200 nm hexagonal platelets (Figure. S10A). In HR-TEM imaging, similar ~100 nm hexagonal platelets were observed with 3.1 Å a-axis spacing, low-Si elemental chemistry, and SAED measurements consistent with fougurite (Figure S3J-L). These SEM and TEM images of the hexagonal platelets were highly similar to those shown in (Halevy et al., 2017). We additionally made a more tentative identification of carbonate green rust in experiments conducted under ferrous conditions at pH 7.5. After aging at 150 °C, SEM and HR-TEM images displayed a rare 150-200 nm hexagonal platelet phase (Figure S2C, 1C) with similar morphology to other observations of green rust, and thus we tentatively interpreted this scarce phase as carbonate green rust. The presence of a Fe[II/III] phase under ferrous conditions may reflect a limited amount of metal-catalyzed oxidation of ferrous hydroxide at high temperatures starting at 150 °C (Shipko and Douglas, 1956), perhaps from residual Fe0 in our ferrous stock solution.

Identification of Iron Oxides:

Electron microscopy-based techniques revealed the presence of iron oxide phases in samples from experiments starting with 5% Fe[III]/FeT. Triangular <100 nm platelets imaged by TEM had 4.8 Å and 2.5 Å d-spacing consistent with magnetite by SAED (Figure S3G,3M; FigureS10D) and were primarily composed of Fe and O (Figure S3; S10G&H). Possibly a different crystal form of magnetite, appeared euhedral in high-temperature precipitates at pH 7.5 (Figure 2J) and in low-temperature precipitates at pH 7.5 (Figure S5D). Bulk XRD analyses confirmed the presence of magnetite in all 5% Fe[III]/FeT samples aged at 150 °C (Figure S4). TEM imaging of 150 °C-aged precipitates at pH 6.5 and 7 also displayed spherule inclusions of ~10 nm in diameter with 2.7Å and 2.5Å d-spacing (Figure 3 L&R), consistent with iron oxide minerals such as hematite. Additional dense phases enriched in Fe and O manifest in 150 °C-aged samples as oblong or globular particles in TEM images (Figure 3I,J&O; Figure S10B,E,F; S11D). The

presence of hematite was additionally indicated by the bulk XRD measurements of 5% Fe[III]/FeT experimental precipitates at pH 6.5 and possibly at pH 7 (Figure S4).

REFERENCES

- ASTM D859-16, 2000, Standard Test Method for Silica in Water: ASTM International, 10.1520/D0859-16.
- Blättler, C.L., Kump, L.R., Fischer, W.W., Paris, G., Kasbohm, J.J., and Higgins, J.A., 2017, Constraints on ocean carbonate chemistry and pCO₂ in the Archaean and Palaeoproterozoic: *Nature Geoscience*, v. 10, p. 41–45, doi:10.1038/ngeo2844.
- Coradin, T., Eglin, D., and Livage, J., 2004, The silicomolybdic acid spectrophotometric method and its application to silicate/biopolymer interaction studies: *Spectroscopy*, v. 18, p. 567–576, doi:https://doi.org/10.1155/2004/356207.
- Dietzel, M., 2000, Dissolution of silicates and the stability of polysilicic acid: *Geochimica et Cosmochimica Acta*, v. 64, p. 3275–3281, doi:10.1016/S0016-7037(00)00426-9.
- Falini, G., Foresti, E., Gazzano, M., Gualtieri, A.F., Leoni, M., Lesci, I.G., and Roveri, N., 2004, Tubular-Shaped Stoichiometric Chrysotile Nanocrystals: *Chemistry – A European Journal*, v. 10, p. 3043–3049, doi:10.1002/chem.200305685.
- Graf, D.L., 1961, Crystallographic tables for the rhombohedral carbonates: *American Mineralogist*, v. 46, p. 1283–1316.
- Guggenheim, S., Bailey, S.W., Eggleton, R.A., and Wilkes, P., 1982, Structural aspects of greenalite and related minerals: *The Canadian Mineralogist*, v. 20, p. 1–18.
- Gunnarsson, I., and Arnórsson, S., 2000, Amorphous silica solubility and the thermodynamic properties of H₄SiO₄ in the range of 0° to 350°C at Psat: *Geochimica et Cosmochimica Acta*, v. 64, p. 2295–2307, doi:10.1016/S0016-7037(99)00426-3.
- Halevy, I., Alesker, M., Schuster, E.M., Popovitz-Biro, R., and Feldman, Y., 2017, A key role for green rust in the Precambrian oceans and the genesis of iron formations: *Nature Geoscience*, v. 10, p. 135–139, doi:10.1038/ngeo2878.
- Halevy, I., and Bachan, A., 2017, The geologic history of seawater pH: *Science (New York, N.Y.)*, v. 355, p. 1069–1071, doi:10.1126/science.aal4151.
- Jiang, C.Z., and Tosca, N.J., 2019, Fe(II)-carbonate precipitation kinetics and the chemistry of anoxic ferruginous seawater: *Earth and Planetary Science Letters*, v. 506, p. 231–242, doi:10.1016/j.epsl.2018.11.010.
- Jones, C., Nomosatryo, S., Crowe, S.A., Bjerrum, C.J., and Canfield, D.E., 2015, Iron oxides, divalent cations, silica, and the early earth phosphorus crisis: *Geology*, v. 43, p. 135–138, doi:10.1130/G36044.1.

- Kinsela, A.S., Jones, A.M., Bligh, M.W., Pham, A.N., Collins, R.N., Harrison, J.J., Wilsher, K.L., Payne, T.E., and Waite, T.D., 2016, Influence of Dissolved Silicate on Rates of Fe(II) Oxidation: *Environmental Science & Technology*, v. 50, p. 11663–11671, doi:10.1021/acs.est.6b03015.
- Maliva, R.G., Knoll, A.H., and Simonson, B.M., 2005, Secular change in the Precambrian silica cycle: Insights from chert petrology: *GSA Bulletin*, v. 117, p. 835–845, doi:10.1130/B25555.1.
- Mizutani, T., Fukushima, Y., Okada, A., Kamigaito, O., and Kobayashi, T., 1991, Synthesis of 1:1 And 2:1 Iron Phyllosilicates and Characterization of Their Iron State by Mössbauer Spectroscopy: *Clays and Clay Minerals*, v. 39, p. 381–386, doi:10.1346/CCMN.1991.0390407.
- Riley, J.P., and Chester, R., 1971, *Introduction to Marine Chemistry*: London, Academic Press, 465 p.
- Shipko, F.J., and Douglas, D.L., 1956, Stability of Ferrous Hydroxide Precipitates: *The Journal of Physical Chemistry*, v. 60, p. 1519–1523, doi:10.1021/j150545a011.
- Siever, R., 1983, Burial History and Diagenetic Reaction Kinetics: *AAPG Bulletin*, v. 67, p. 684–691, doi:10.1306/03B5B67D-16D1-11D7-8645000102C1865D.
- Siever, R., 1992, The silica cycle in the Precambrian: *Geochimica et Cosmochimica Acta*, v. 56, p. 3265–3272, doi:10.1016/0016-7037(92)90303-Z.
- Spencer, R.J., and Hardie, L.A., 1990, Control of seawater composition by mixing of river waters and mid-ocean ridge hydrothermal brines, *in* Spencer, R.J. and Chou, I. eds., *Fluid-Mineral Interactions: A Tribute to H. P. Eugster*, Saint Louis, MO, The Geochemical Society, v. Special Publication No. 2, p. 409–419.
- Stefurak, E.J.T., Lowe, D.R., Zentner, D., and Fischer, W.W., 2015, Sedimentology and geochemistry of Archean silica granules: *GSA Bulletin*, v. 127, p. 1090–1107, doi:10.1130/B31181.1.
- Stookey, L.L., 1970, Ferrozine---a new spectrophotometric reagent for iron: *Analytical Chemistry*, v. 42, p. 779–781, doi:10.1021/ac60289a016.
- Stüeken, E.E., 2016, Nitrogen in Ancient Mud: A Biosignature? *Astrobiology*, v. 16, p. 730–735, doi:10.1089/ast.2016.1478.
- Viollier, E., Inglett, P.W., Hunter, K., Roychoudhury, A.N., and Van Cappellen, P., 2000, The ferrozine method revisited: Fe(II)/Fe(III) determination in natural waters: *Applied Geochemistry*, v. 15, p. 785–790, doi:10.1016/S0883-2927(99)00097-9.

SUPPLEMENTAL FIGURES AND TABLES

Table S1: Artificial seawater solution composition per 500mL of degassed ultrapure water.

Chemical Component, Chemical Formula	Concentration (mM)
Sodium chloride, NaCl	400
Sodium bicarbonate, NaHCO ₃	22
Magnesium chloride hexahydrate, MgCl ₂ * 6H ₂ O	20
Ammonium chloride, NH ₄ Cl	10
Potassium chloride, KCl	7
Sodium orthosilicate, Na ₄ SiO ₄	1
Ferrous chloride, FeCl ₂	0.95-1
Ferric chloride, FeCl ₃	0-0.05

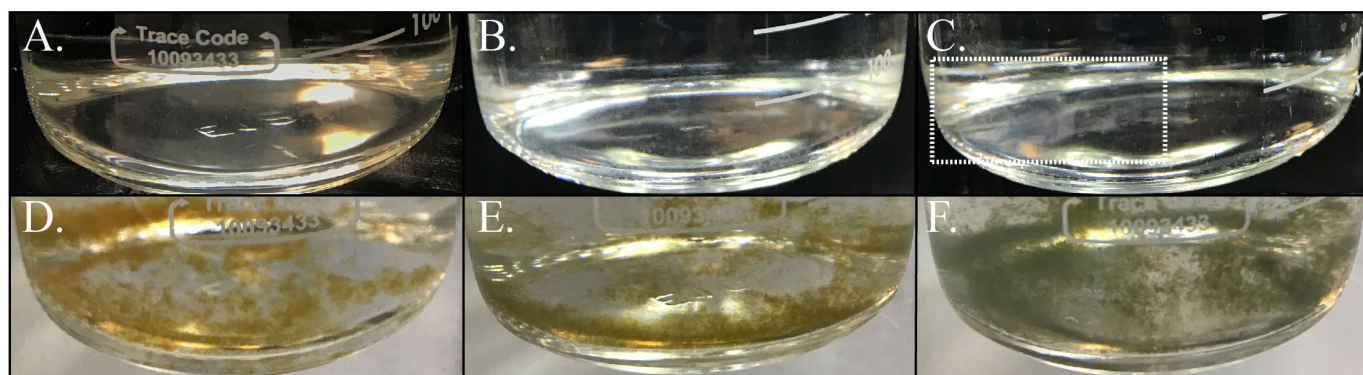


Figure S1: Experiments after 5 days at 25 °C with 0% Fe[III]: at pH 6.5 (A), pH 7.0 (B), and pH 7.5 (C). Distinct white, wispy material at pH 7.5 is indicated in the dashed box (C). The addition of 5% Fe[III] at 25 °C produced an orange precipitate at pH 6.5 (D), an orange-green precipitate at pH 7.0 (E), and a green precipitate at pH 7.5 (F).

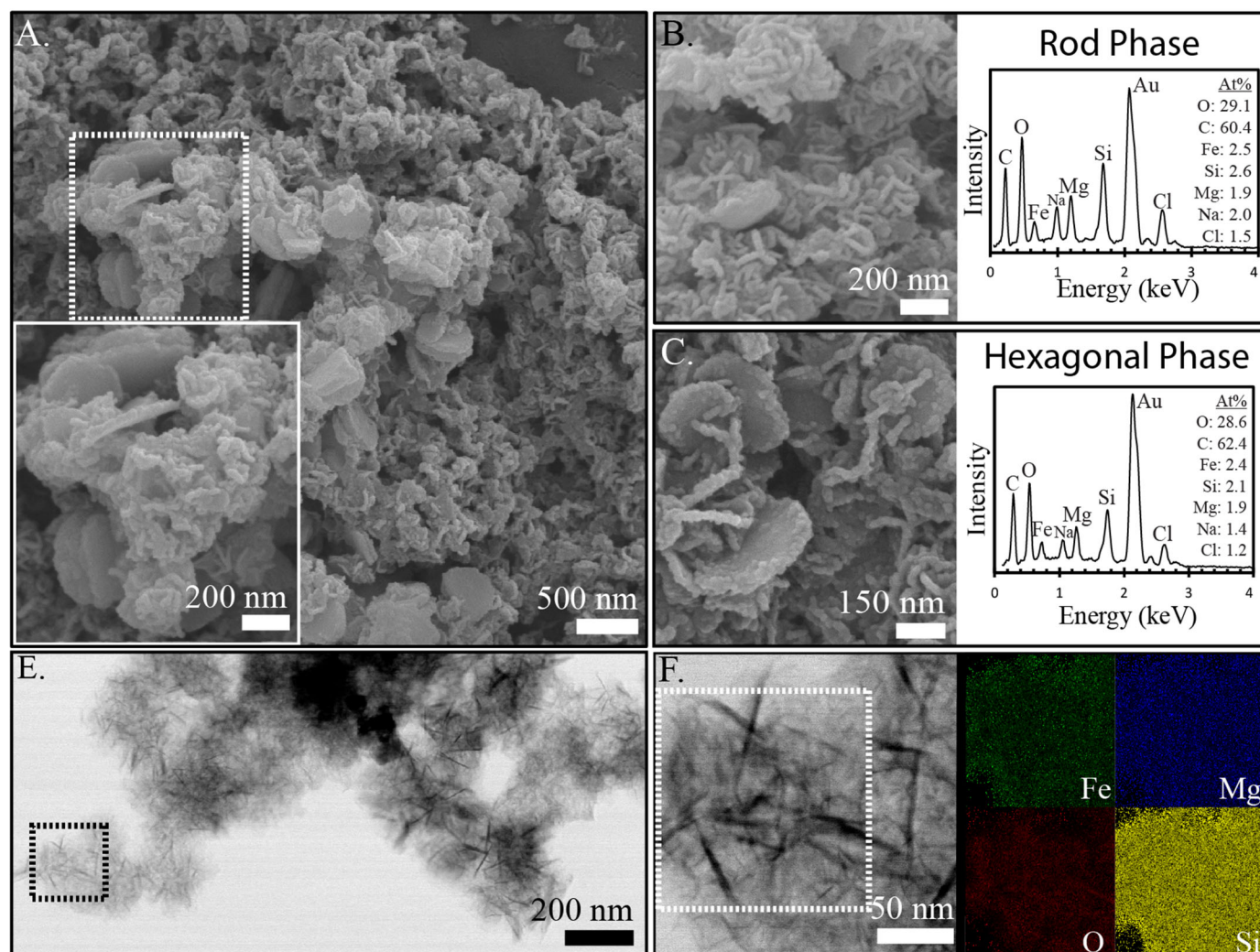


Figure S2: After 5 days at 150 °C, ferrous experimental precipitates at pH 7.5 displayed two distinct phases by SEM imaging (A): <100 nm rods composed mostly of O, Fe, Si, and Mg (B) and 100-200 nm hexagonal platelets with high Fe & O similar to green rust carbonate (C). TEM imaging showed abundant poorly-ordered structures (E) where HR-TEM was not able to capture clear lattice spacing of most particles (F, but see Fig. 1F for exception) but the elemental chemistry and one instance of lattice spacing was similar to an iron-magnesium silicate (F, elemental maps).

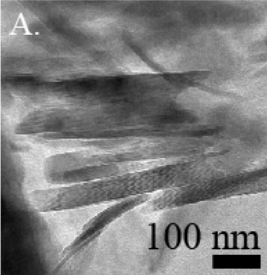
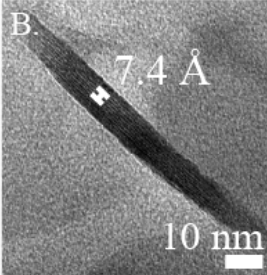
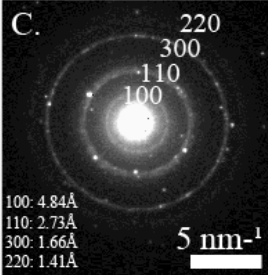
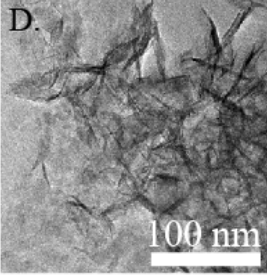
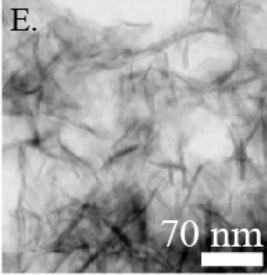
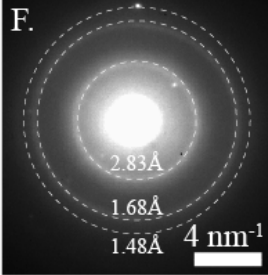
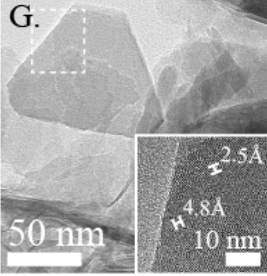
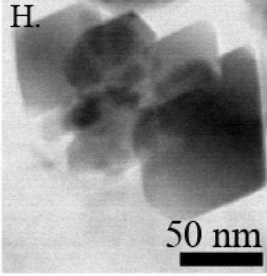
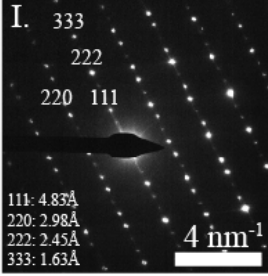
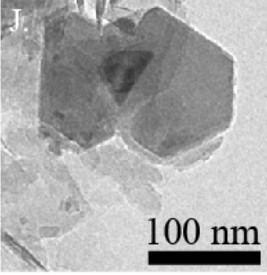
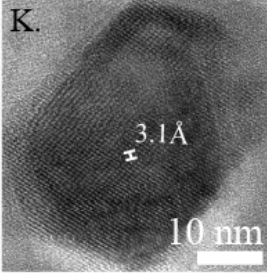
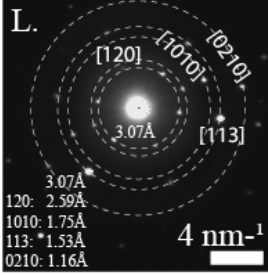
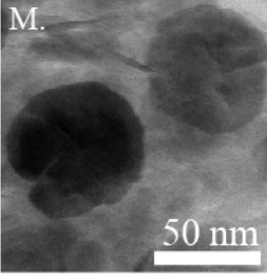
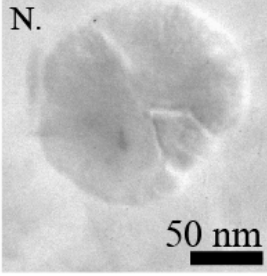
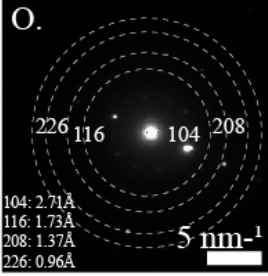
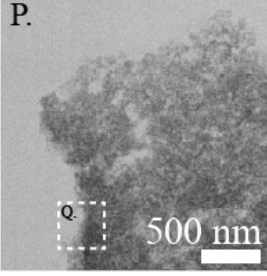
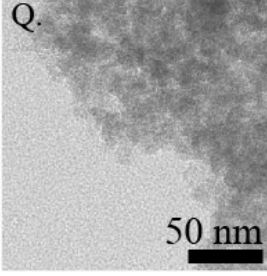
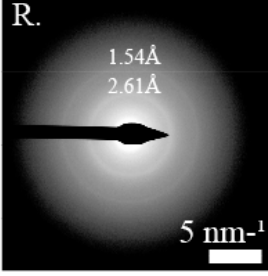
TEM Bright Field Image	Diffraction Pattern	Rep. Atomic%	Rep. Fe:Mg	Rep. Fe+Mg/Si
A. 	B. 	C. 	5% Fe(III) pH 6.5: 25°C 150°C O: 56.7 56.9 Fe: 16.4 12.0 Si: 15.4 16.4 Mg: 11.5 14.7	5% Fe(III) pH 6.5: 25°C 150°C 1.8 1.6
D. 	E. 	F. 	Fe(II) pH 7.5: 150°C O: 47.0 Fe: 17.0 Si: 25.1 Mg: 10.9	Fe(II) pH 7.5: 1.6 (150°C) 1.1 (150°C)
G. 	H. 	I. 	5% Fe(III) pH 7.5: 25°C 150°C O: 55.1 58.8 Fe: 17.2 11.8 Si: 24.1 16.5 Mg: 3.6 12.9	5% Fe(III) pH 7.5: 25°C 150°C 4.8 0.9 0.9 1.5
J. 	K. 	L. 	Magnetite: 25/150°C O: 48.8 Fe: 40.6 Si: 7.7 Mg: 2.9	
M. 	N. 	O. 	Green Rust Carbonate: 150°C O: 57.1 Fe: 31.4 Si: 4.7 Mg: 6.8	
P. 	Q. 	R. 	Hematite: 150°C O: 57.5 Fe: 27.7 Si: 7.4 Mg: 7.4	
			Amorphous: 25°C O: 51.9 Fe: 32.4 Si: 14.6 Mg: 1.1	Amorphous: 25°C 29.5 2.3

Figure S3: Compilation of representative morphological, structural, and chemically distinct phases present across the range of experimental conditions (pH 6.5-7.5, 0-5% Fe[III]/FeT) and aged at 25 or 150°C. At pH 6.5-7 with 5% Fe[III]/FeT, TEM images of 100 nm stacks of well-ordered particles (A) exhibiting ~ 7.4 Å basal spacing (B) with a polynanocrystalline diffraction pattern (C) and elemental chemistry (right) consistent with a 1:1 silicate like high magnesium greenalite. At pH 7.5 with 5% Fe[III]/FeT, TEM displayed abundant < 50 nm curling structures (D) where HR-TEM was not able to capture clear lattice spacing of most particles (E, but see Fig. 2K for exception) with an amorphous diffraction pattern (F) and an elemental chemistry suggesting a poorly-ordered silicate. At all pHs, TEM captured 50-70 nm triangular particles with 2.5 Å and 4.8 Å spacing (G) or euhedral morphology (H) with a highly crystalline diffraction pattern (I) and elemental chemistry consistent with an iron-oxide, magnetite. Another phase observed by TEM at pH 6.5-7.5 were 100 nm hexagonal platelets (J) with 3.1 Å spacing (K) a crystalline diffraction pattern (L) and elemental chemistry consistent with carbonate green rust. At pH 6.5, TEM revealed dense 50 nm spherules (M-N) with a crystalline diffraction pattern (O) and elemental chemistry similar to the iron oxide hematite. At all pHs, TEM images showed abundant amorphous material (P-Q) after low temperature aging at 25°C with a highly-amorphous diffraction pattern (R) with an elemental chemistry for an iron and silica-rich amorphous phase.

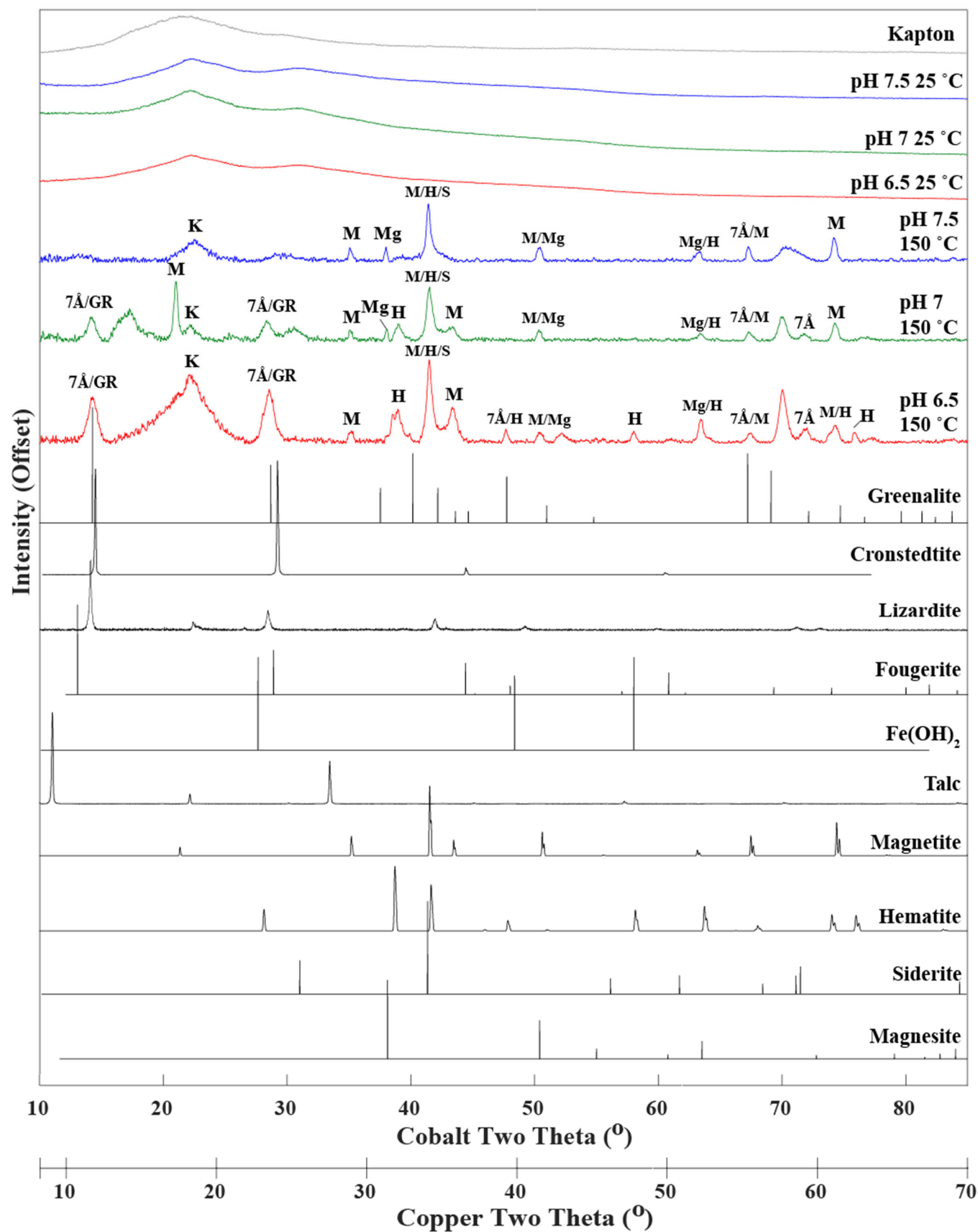


Figure S4: Cobalt-sourced XRD diffraction pattern of room temperature (25 °C) and high temperature (150 °C) aged samples run in Kapton tubes. For comparison, also shown are: a blank Kapton tube (K); 1:1 clay minerals with 7Å basal spacing [Greenalite, $(\text{Fe}^{2+}, \text{Fe}^{3+})_{2-3}\text{Si}_2\text{O}_5(\text{OH})_4$ (Guggenheim et al., 1982); Cronstedtite, $(\text{Fe}^{2+}, \text{Fe}^{3+})_3(\text{Si}, \text{Fe}^{3+})_2\text{O}_5(\text{OH})_4$ (Lab Standard); Lizardite, $(\text{Mg}_3\text{Si}_2\text{O}_5(\text{OH})_4$ (RRUFF-R060006)]; Fougerite, a natural carbonate green rust [$\text{Fe}^{(2+)}_4\text{Fe}^{(3+)}_2(\text{OH})_{12}\text{CO}_3 \cdot 3\text{H}_2\text{O}$ (RRUFF-0012240)]; iron(II) hydroxide [$(\text{Fe}(\text{OH})_2$ (ICDD PDF #013-0089)]; a 2:1 clay mineral with 10Å basal spacing [Talc, $\text{Mg}_3\text{Si}_4\text{O}_{10}(\text{OH})_2$ (RRUFF-R040137)]; iron oxides [Magnetite, $\text{Fe}^{2+}, \text{Fe}^{3+}_2\text{O}_4$ (RRUFF-R061111) and Hematite, Fe_2O_3 (RRUFF-R110013)], and carbonates [Siderite, FeCO_3 (RRUFF-0020837) Magnesite, MgCO_3 (Graf, 1961)]. An axis with copper two theta values is included to facilitate comparisons to other datasets.

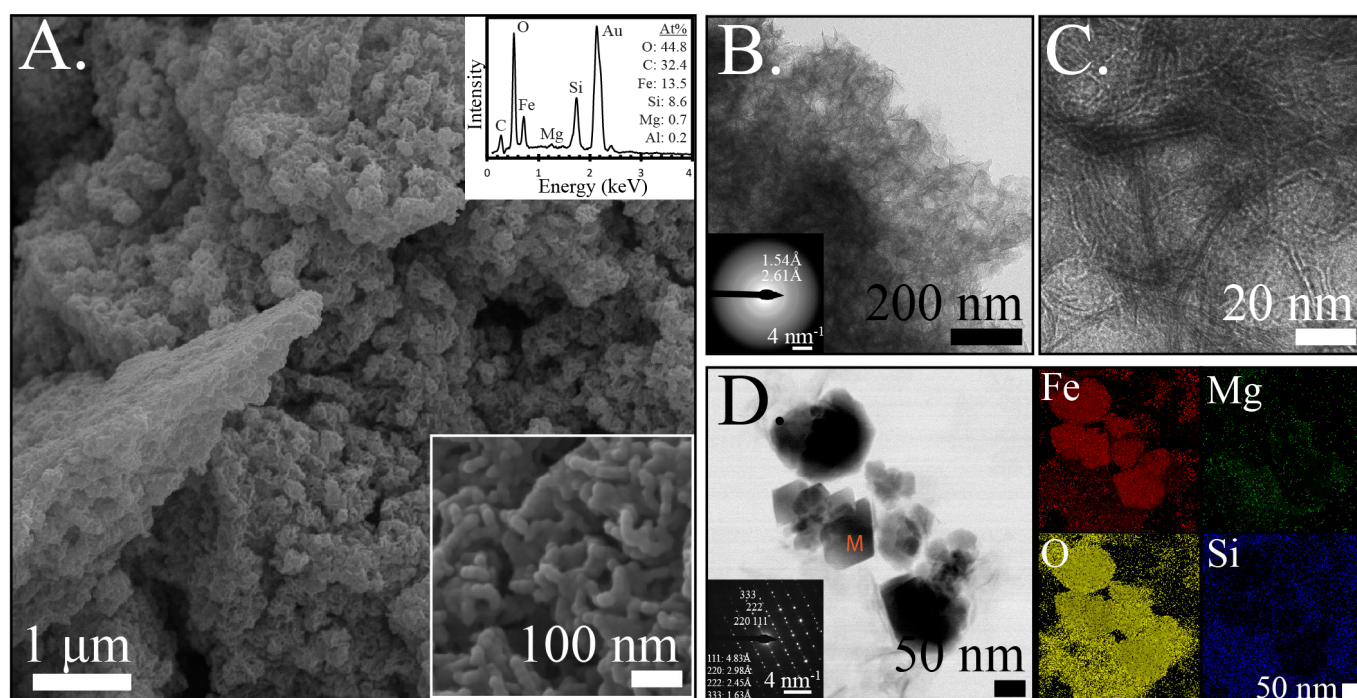


Figure S5: Experimental precipitate with 5% Fe[III]/FeT at pH 7.5 after 5 days at 25 °C displayed tubular morphologies by SEM imaging (A), with ~75 nm rods composed of primarily O, Fe, and Si, with low Mg and Al (Au from gold coating). TEM imaging showed poorly-ordered structures (B) accompanied by an amorphous diffraction pattern (B-inset) where no layer spacing information was obtained by HR-TEM (C). Localized zones contained dense euhedral minerals, likely iron oxides or nano-scale magnetite as indicated by diffraction and elemental data (D, D-inset).

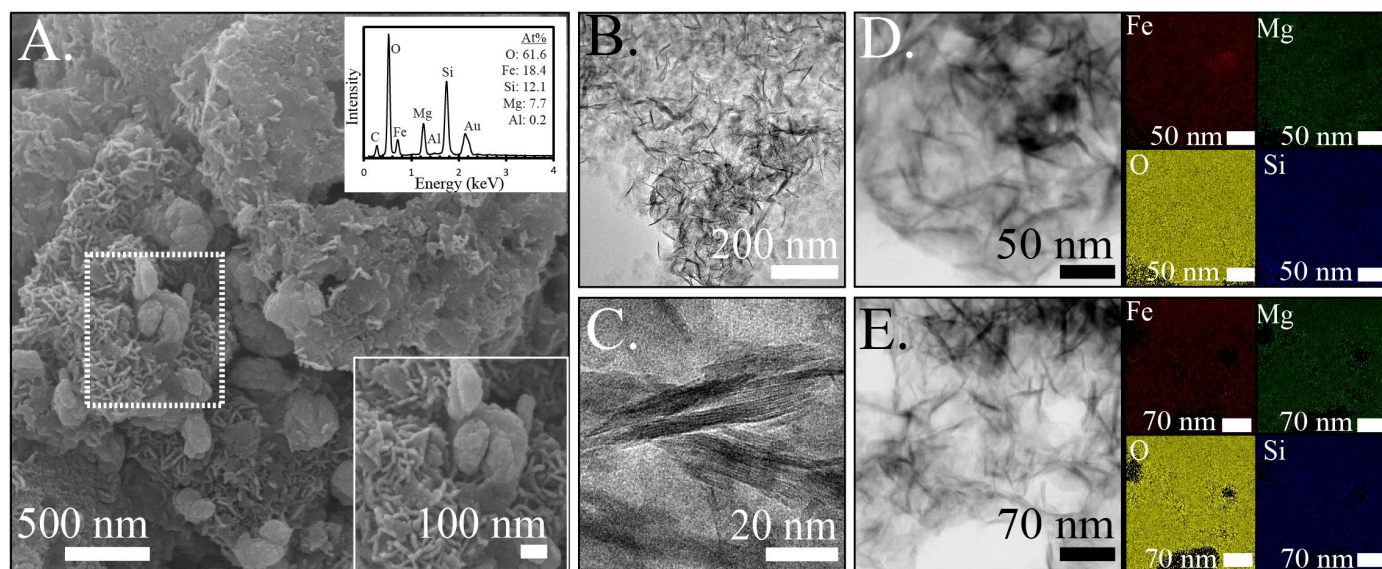


Figure S6: After the 5% Fe[III]/FeT at pH 7.5 precipitates underwent 150 °C aging, SEM imaging of the precipitates revealed ~100 nm tube-like phases and ~200-300 nm oblong structures (A). TEM images displayed poorly-ordered layered structures (B) where HR-TEM was not able to capture clear lattice spacing of most particles (C, but see Fig. 1Q for exception) but the elemental chemistry was similar to an iron-magnesium silicate (D & E).

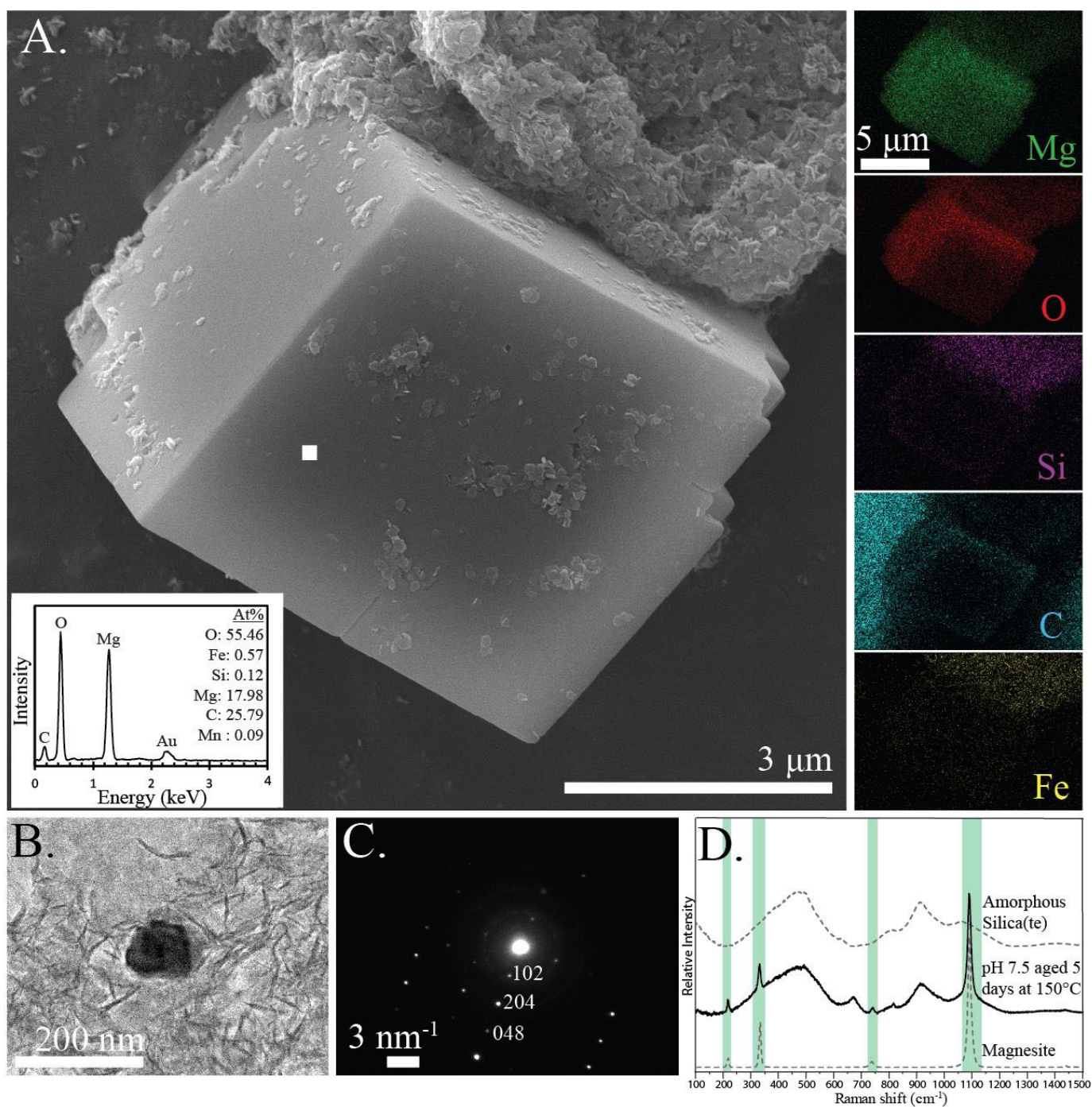


Figure S7: High temperature formation of magnesite. An SEM image of a 5 μm rhombohedral magnesite crystal imaged from a 5% Fe[III]/FeT experiment at pH 6.5 after 150 $^{\circ}\text{C}$ aging. SEM EDS point spectrum indicated by white square symbol (A-inset) and elemental maps (right) of magnesite crystal. TEM image from 150 $^{\circ}\text{C}$ -aged 5% Fe[III]/FeT sample at pH 7.5 of dense crystal surrounded by elongated silicate phases (B) with crystal confirmed as magnesite by SAED pattern (C). Raman measurements of the same sample plotted in black (D) compared to the magnesite RRUFF standard and lab-synthesized standard of amorphous silica(te).

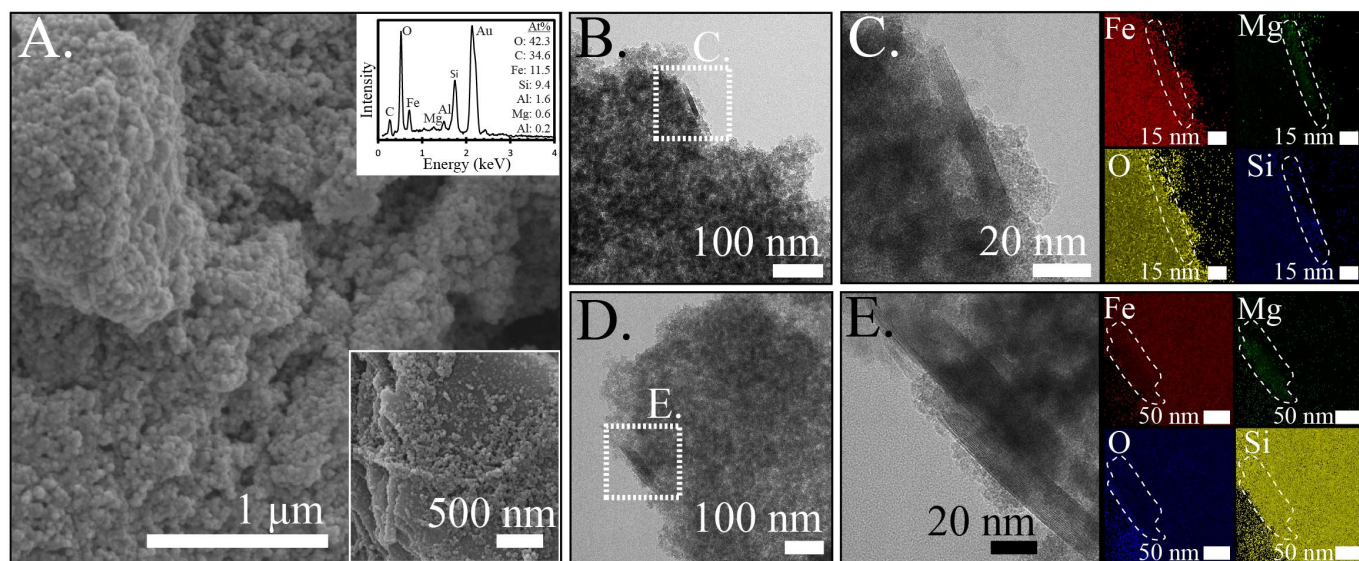


Figure S8: Precipitates formed with 5% Fe[III]/FeT at pH 6.5 after 5 days at 25 °C were dominated by aggregates of microgranules, as imaged by SEM (A). TEM imaging showed abundant amorphous precipitates (B & D) but also revealed rare occurrences of well-ordered 7 Å layered structures (C & E) with an iron-magnesium silicate-like chemistry.

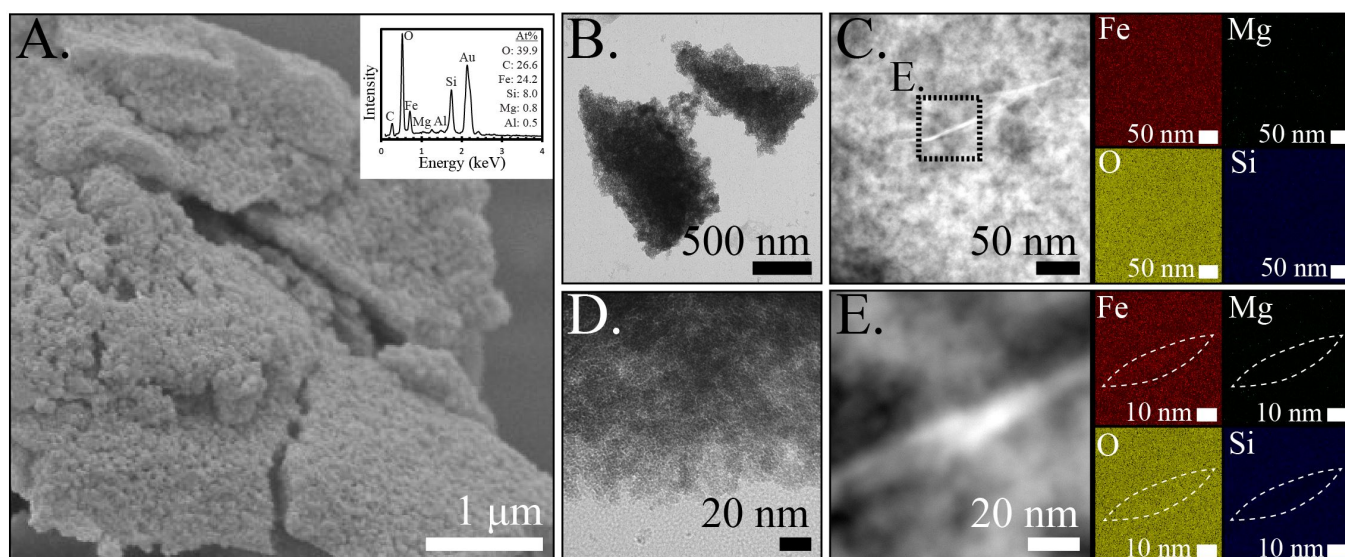


Figure S9: Precipitates formed with 5% Fe[III]/FeT at pH 7 after 5 days at 25 °C displayed a microgranular texture with SEM imaging (A). Amorphous material was observed on the nano-scale by TEM imaging (B, D) with rare needle-like structures (C, E). The thin wavy structure (C) was not compositionally distinct from the surrounding and overlying material by HAADF (C, E).

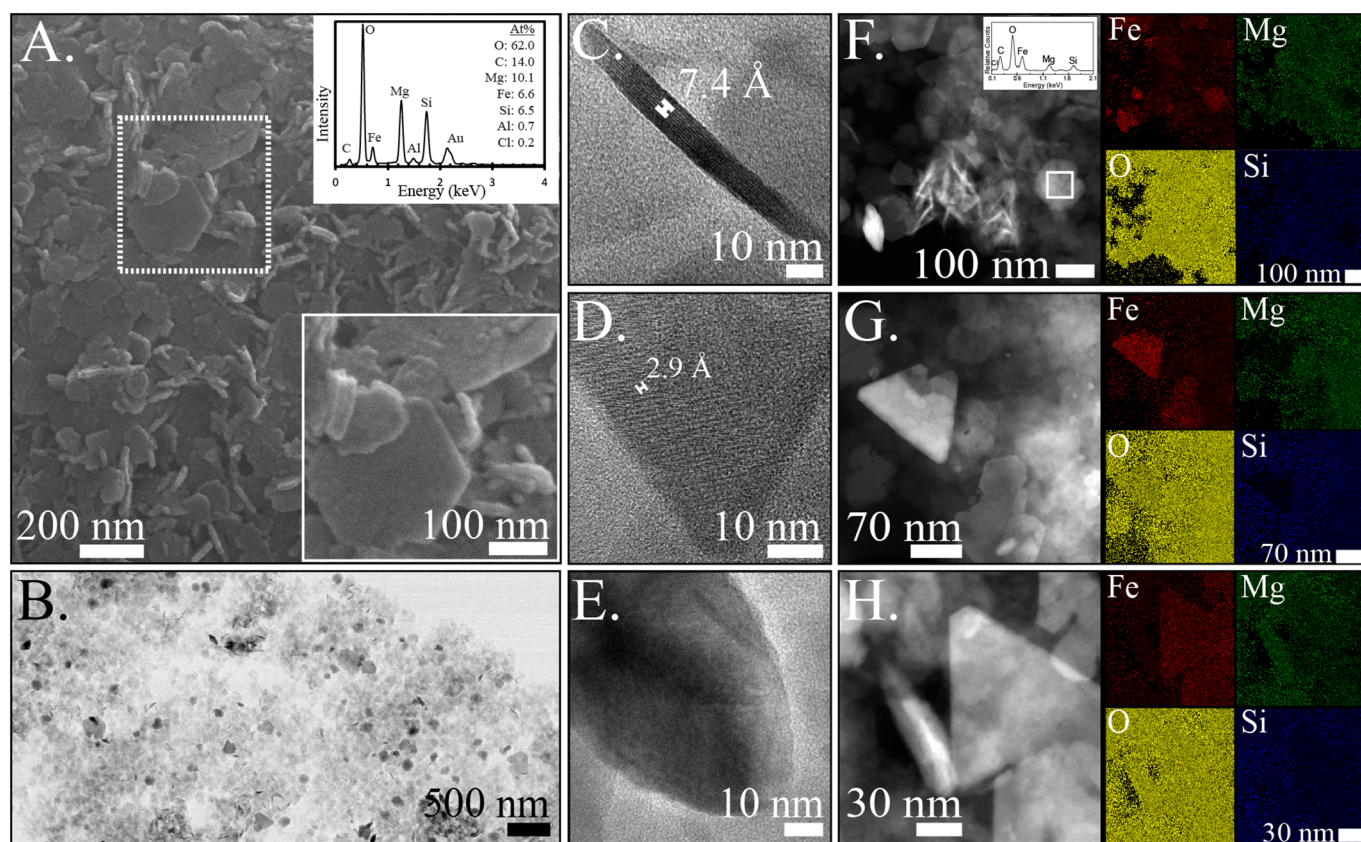


Figure S10: After 150 °C aging, precipitates formed in 5% Fe[III]/FeT at pH 6.5 showed mixed morphologies by SEM imaging, with abundant ~200 nm hexagonal platelets (likely carbonate green rust) and <100 nm rods (A). TEM imaging (B) also displayed a mixture of morphologically distinct phases: green rust (large gray crystals), well-ordered 7 Å iron-magnesium silicates (C, F), nano-scale triangular magnetite platelets with 2.96 Å spacing (D) with high Fe and O (G, H), and dense iron oxide minerals (E) that were composed largely of Fe and O (F).

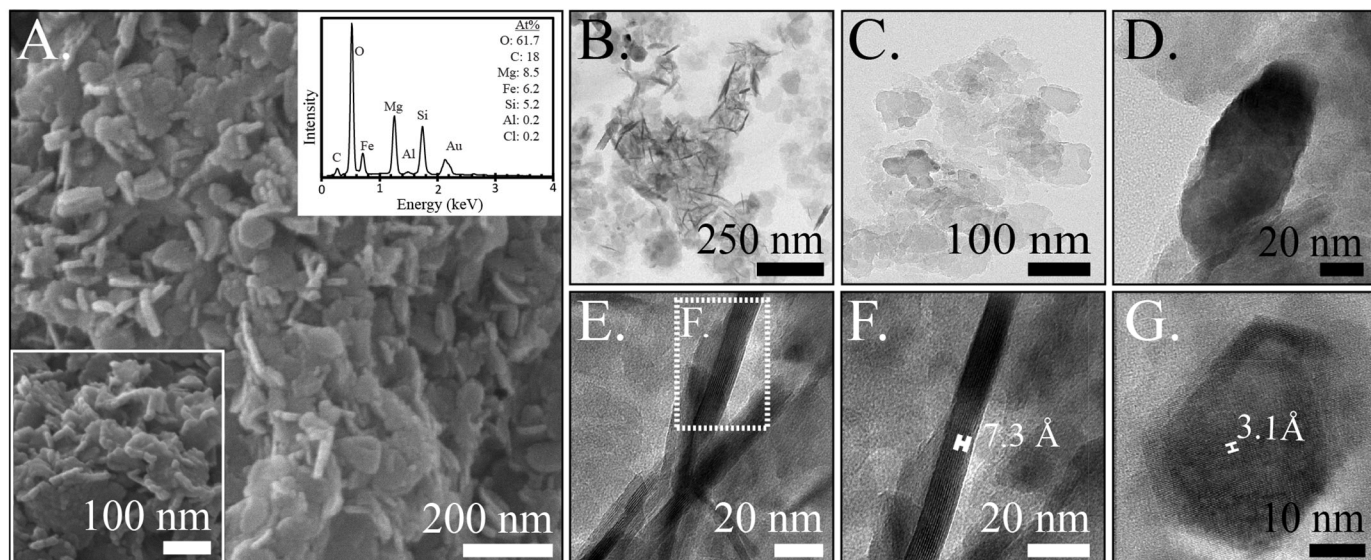


Figure S11: Precipitates from 5% Fe[III]/FeT experiments at pH 7 after 150 °C aging contained <100 nm rod-like structures and ~100 nm platelets in SEM imaging (A). TEM imaging revealed a mixture of nanometer-scale phases (B): amorphous material (C), <100 nm dense oblong phase (D), well-ordered silicates (E) with 7 Å lattice spacing measured by HR-TEM (F), and <50 nm hexagonal platelets with 3.1 Å spacing consistent with carbonate green rust (G).